

Pattern Recognition in the CKM Detector

Stephen R Steffes

Project Advisor: Myron Campbell

Department of Physics, University of Michigan

Ann Arbor, Michigan 48109, U.S.A.

November 26, 2001

Abstract

The CKM experiment hopes to measure $|V_{td}|$ to 10%. To introduce the experiment, we first discuss the theory of CP violation starting from its discovery in 1964 up until the present KM theory. We then introduce the goals and methods of the CKM experiment and introduce the DMS. We present a pattern recognition algorithm for the DMS using simulated data. The results of which will be discussed at the end.

Contents

1	Introduction	4
2	CP Violation Theory	4
2.1	The C, P and T symmetries	4
2.2	The Neutral Kaon System	5
2.3	Symmetry Violation in the Neutral Kaon System	7
2.4	The Cabibbo Theory	8
2.5	KM Theory and the CKM Matrix	9
3	The CKM Experiment	13
3.1	The DMS	16
4	Pattern Recognition in the DMS	17
4.1	The Algorithm	17
4.2	Results	25
4.2.1	Momentum Resolution	25
4.2.2	Track Finding Efficiency	25
4.2.3	Timing	26

List of Figures

1	(a) A square is symmetric under 90 degree rotations, clockwise or counter clockwise, about its center. (b) It is also symmetric under reflections in any of the four axes drawn.	4
2	Two different bases for the xy-plane.	7
3	The six unitarity triangles as presented in [1]. The triangles on the left are from (17) and the ones on the right are from (16).	11
4	The simplified db unitarity triangle.	11
5	Constraints in the $(\bar{\rho}, \bar{\eta})$ plane for the most relevant observables as presented in [2].	12
6	The current measured constraints on $\bar{\rho}$ and $\bar{\eta}$ as presented in [3].	12
7	A possible outcome for constraints on $\bar{\rho}$, $\bar{\eta}$ and β obtained from future experiments, as presented in [3].	14

8	The CKM detector as presented in [3]. The lower section (when viewed as landscape) shows the true proportions of the detector.	15
9	Two layers of straws, one primed and one unprimed, seen from end on. The dot in the center of each tube is the wire.	16
10	100,000 randomly distributed numbers using “white_noise”.	19
11	A histogram of $ (\sum drift\ distance) - (straw\ radius) $ for $\sim 56,000$ pairs of hits, fit to a gaussian distribution.	19
12	A histogram of $ \frac{x+y}{\sqrt{2}} - u $ for $\sim 10,000$ good DMS crossing, fit to a gaussian distribution.	19
13	A histogram of $ \frac{x-y}{\sqrt{2}} - v $ for $\sim 8,000$ good DMS crossing, fit to a gaussian distribution.	19
14	$\chi^2/degree$ distribution for DMS1.	21
15	$\chi^2/degree$ distribution for DMS2-4.	21
16	Initial particle momentums from a simulated CKM beam as obtained from [3].	23
17	Histogram of reconstructed momentums of ~ 4000 events with initial momentum of $23\text{GeV}/c$	23
18	$\chi_y^2/degree$ distribution for ~ 3000 good events with 29 hits per event.	24
19	Close up of Figure 18.	24
20	$\chi^2/degree$ distribution for ~ 3000 good events with 29 hits per event.	24
21	Close up of Figure 20.	24
22	Histogram of (calculated p - average actual p) for ~ 5000 tracks.	25
23	Track finding efficiency of 4400 events with one kaon per event.	27
24	Track finding efficiency of 1000 events with two kaons per event.	27
25	Track finding efficiency of 1000 events with four kaons per event.	28
26	Track finding inefficiency due to particles hitting the outer wall of the beam pipe.	28
27	Average runtime vs. the number of hits per event. The data is fit to an exponential; the equation of the fit is on the graph.	29

List of Tables

1	The three discrete symmetries and their results.	5
---	--	---

1 Introduction

The CKM experiment is a particle physics experiment which plans to run at FNAL in 2006. The main goal of the experiment is to measure the amount of CP violation that comes from the CKM matrix by measuring one element of the matrix to 5%. The research done uses Monte Carlo data from a simulated CKM detector to test the track finding and momentum measuring capabilities of the DMS portion of the detector. We first give an overview of the physics behind the CKM experiment and then discuss the experiment itself. Lastly, we discuss the research done on the pattern recognition algorithm and its results.

2 CP Violation Theory

2.1 The C, P and T symmetries

Symmetry is a property of a geometrical object in which the object is indistinguishable before and after certain operations are applied. For example (Figure 1), a square is symmetric under 90 degree rotations and under reflections in any of the four axes drawn in Figure 1 (b).

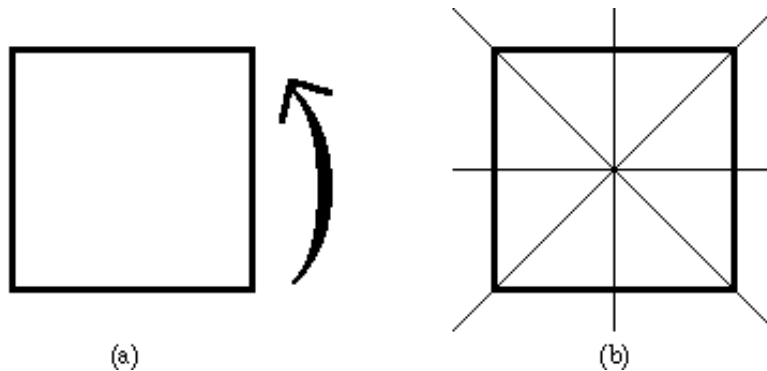


Figure 1: (a) A square is symmetric under 90 degree rotations, clockwise or counter clockwise, about its center. (b) It is also symmetric under reflections in any of the four axes drawn.

Mathematical equations also have symmetries. Parity is an operation where each point is reflected about the origin. For example, if we apply the

parity operator, P, on the functions $f(x) = x^2$, $g(x) = x$ and $h(x) = x + b$, we get

$$Pf(x) = f(-x) = (-x)^2 = x^2 = f(x) \quad (1)$$

$$Pg(x) = g(-x) = -x = -g(x) \quad (2)$$

$$Ph(x) = h(-x) = -x + b. \quad (3)$$

The equation $f(x)$ is said to have even symmetry under parity because $Pf(x) = f(x)$. Similarly, $g(x)$ is said to have odd symmetry under parity because $Pg(x) = -g(x)$ and $h(x)$ does not have any symmetry under parity because $h(x) \neq Ph(x) \neq -h(x)$.

There are three discrete symmetries in particle physics: charge conjugation, parity and time reversal. The charge conjugation operator, C, changes all particles into their antiparticles and vice versa, the parity operator, P, reflects all points about the origin (as described above) and the time reversal operator, T, reverses the direction of time. There are also combinations of symmetries, CP and CPT, which combine the appropriate operations. These symmetries are summed up in Table 1.

Operation	Result
C	<i>particle</i> \rightarrow <i>antiparticle</i>
P	$\vec{x} \rightarrow -\vec{x}$
T	$t \rightarrow -t$
CP	<i>particle</i> \rightarrow <i>antiparticle</i> $\vec{x} \rightarrow -\vec{x}$
CPT	<i>particle</i> \rightarrow <i>antiparticle</i> $\vec{x} \rightarrow -\vec{x}$ $t \rightarrow -t$

Table 1: The three discrete symmetries and their results.

2.2 The Neutral Kaon System

All particles have a corresponding antiparticle. The main difference between a particle and its antiparticle is that they have opposite charges; the electron's (-1e) antiparticle is the positron (+1e), the proton's (+1e) antiparticle is the antiproton (-1e). Neutral particles are a different story. Some neutral

particles are their own antiparticles, while some have a separate distinguishable antiparticle; the photon, π^0 and Z^0 are all their own antiparticles, while the neutron and K^0 have antiparticles.

The K^0 was discovered in 1946 by Rochester and Butler [4], while looking at cosmic radiation. The K^0 consists of a d quark and an \bar{s} quark. It is special in that it has a high rate of production but a significantly long lifetime. At the time of its discovery, this was an unusual characteristic; only a few other particles behaved in such a manner. To try to explain the K^0 's strange behavior, Nakano and Nishijima [5] and, independently, Gell-Mann [6] came up with a particle classification scheme that assigned a “strangeness” quantum number of $S=0$ for the u and d quarks and $S=-1$ to the s quark. This grouped the K mesons into two doublets, those with $S=1$, K^+ and K^0 , and their antiparticles with $S=-1$, K^- and \bar{K}^0 , instead of the normal assignment of a triplet, K^+ , K^- and K^0 . Strangeness was then conserved in strong interactions, when producing K mesons, and violated in weak interactions, when K mesons decay. The K^0 could only decay by strangeness-violating weak decays, thus “explaining” its slow decay.

Assigning the K mesons into two doublets made the K^0 and \bar{K}^0 distinct particles. However, both particles could decay into $\pi^+\pi^-$ as observed. Apparently, there was no measurable difference between them. But there was a contradiction because the K^0 and \bar{K}^0 were distinct particles. In 1955, Gell-Mann and Pais proposed a solution [7]. They said that the source of the $\pi^+\pi^-$ final state must be from a linear combination of K^0 and \bar{K}^0 . They noticed that $\pi^+\pi^-$ is even under C ; if we exchange particle with antiparticle then $\pi^+\pi^- \rightarrow \pi^-\pi^+$. This $\pi^+\pi^-$ must come from an initial particle state of $K^0 + \bar{K}^0$. The other particle state then must be $K^0 - \bar{K}^0$ which is odd under C and is therefore forbidden to decay to $\pi^+\pi^-$. This second particle could, however, decay to three body states such as $\pi^+\pi^-\pi^0$ and $\pi^0\pi^0\pi^0$, which are odd under C , thus having a much longer lifetime. In 1956, the K_2 was looked for and found at the Brookhaven cosmotron by a Columbia group [8]. These two particles were called K_1 and K_2 respectively and, after normalizing, their wave functions were defined as

$$K_1 = \frac{K^0 + \bar{K}^0}{\sqrt{2}} \quad (4)$$

$$K_2 = \frac{K^0 - \bar{K}^0}{\sqrt{2}}. \quad (5)$$

The neutral K system is a degenerate two-state system, like a pair of

coupled pendulums, polarized light or a two dimensional plane. If we look at a two dimensional plane, there are infinitely many orthonormal bases to choose from and all choices are equal. Any basis describes the whole system and they are all indistinguishable. For example (Figure 2), in (a) the basis is the vectors \hat{x} and \hat{y} which is indistinguishable from the vectors $\frac{\hat{x}+\hat{y}}{\sqrt{2}}$ and $\frac{-\hat{x}+\hat{y}}{\sqrt{2}}$ in (b); the vectors in (a) and (b) differ by a 45 degree rotation. With linear combinations of the vectors in (a) or in (b), we can make any vector in the xy-plane.

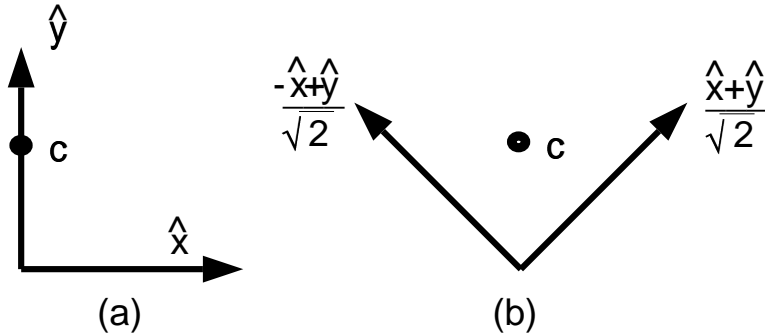


Figure 2: Two different bases for the xy-plane.

Just like we can represent any direction using either the two vectors in Figure 2 (a) or in (b), we can represent any wave function in the neutral K system using either K^0 and \bar{K}^0 or K_1 and K_2 , but one choice is simpler than the other. If we take the point c , the vectors in (a) corresponds to the eigenstates of the system. The basis in (b) is like the $K^0 \bar{K}^0$ system, while the basis in (a) is like the $K_1 K_2$ system. Neutral kaons are produced in a state like that of (b) and decay in a state like (a) with the point c corresponding to the $\pi^+ \pi^-$ state.

2.3 Symmetry Violation in the Neutral Kaon System

In 1957, with the combined evidence of many experiments, it was discovered that only the right-handed antineutrino ($\bar{\nu}_R$) and the left-handed neutrino (ν_L) existed; the ν_R and the $\bar{\nu}_L$ are not involved in weak interactions. Therefore the weak force violates P because $P\bar{\nu}_R = \bar{\nu}_L$ and $P\nu_L = \nu_R$ and it violates C because $C\bar{\nu}_R = \nu_R$ and $C\nu_L = \bar{\nu}_L$. Although, the weak force is still CP invariant because $CP\nu_L = \bar{\nu}_R$. If we apply CP to K_1 and K_2 we get

$CP(K_1) = K_1$ and $CP(K_2) = -K_2$, so the decay modes of the K_1 and K_2 remain the same as previously stated.

Then, a group at Brookhaven found evidence of $K_2 \rightarrow \pi^+\pi^-$ [9] in 1964. They measured $\Gamma(K_2 \rightarrow \pi^+\pi^-) \sim 2 \times 10^{-3}$ and $\Gamma(K_2 \rightarrow \pi^0\pi^0) \sim 10^{-3}$, where Γ is the branching ratio or the probability of decay. These decays clearly violate CP. Therefore the states of definite mass and lifetime for the neutral kaon are “K short” and “K long”, K_S and K_L respectively, where

$$K_S \simeq K_1 + \epsilon K_2 \quad (6)$$

$$K_L \simeq K_2 + \epsilon K_1. \quad (7)$$

Here, ϵ (sometimes called ϵ_K) is a parameter describing CP violation. The current measured value is $\epsilon = (2.271 \pm .017) \times 10^{-3} e^{i(43.49 \pm .08^\circ)}$ [10]. ϵ is said to be a measure of indirect CP violation because it is the mixture of CP eigenstates (K_1 and K_2) which violates CP and not an eigenstate alone. The Standard Model (SM) of particle physics predicts that there is also direct CP violation in which a single CP eigenstate violates CP. ϵ' is the parameter describing direct CP violation. Current related measurements are $\epsilon'/\epsilon = (2.1 \pm .5) \times 10^{-3}$ and $\phi(\epsilon') = 48 \pm 4^\circ$ [10].

For many years ϵ was the only parameter describing CP violation and no theory could explain why it was there; it was unclear whether ϵ' was non-zero. Many theories proposed that CP violation came from weak-interaction couplings of particles with masses on the order of the mass of the W boson: the Kobayashi-Maskawa model and the Weinberg model are the most famous. There was also the possibility of a ‘superweak’ origin, where CP violation comes from a hard coupling which only affects $K^0 - \bar{K}^0$ mixing.

2.4 The Cabibbo Theory

At one time it was thought that the u would only couple (emit or absorb) with the d and not the s . When decays like $K^+ \rightarrow \mu^+\nu_\mu$ were discovered, the former theory had to be changed because the K^+ is composed of a u and an \bar{s} which means this decay couples the u and \bar{s} . To account for these weak decays of s quarks, Cabibbo provided a theory of quark mixing between the u , d and s quarks, in 1963 [11]. Later, after Glashow, Iliopoulos and Maiani proposed its existence [12], the c quark was added to Cabibbo’s theory.

Just like the K^0 and \bar{K}^0 can mix to form K_1 and K_2 , Cabibbo’s model allows the d and s quarks to mix and form d' and s' . In this model, the u

only couples with the d' and the c only couples with the s' . The d' and s' must be normalized linear combinations of d and s , which means

$$d' = d\cos\theta_c + s\sin\theta_c \quad (8)$$

$$s' = -d\sin\theta_c + s\cos\theta_c \quad (9)$$

or in matrix form

$$\begin{pmatrix} d' \\ s' \end{pmatrix} = \begin{pmatrix} \cos\theta_c & \sin\theta_c \\ -\sin\theta_c & \cos\theta_c \end{pmatrix} \begin{pmatrix} d \\ s \end{pmatrix}. \quad (10)$$

Where θ_c is an arbitrary parameter called the quark mixing angle, or the Cabibbo angle. The current value of $\sin\theta_c = .2196 \pm .0023$ [10]. Equation (10) is just a rotation of the (d, s) vector to the (d', s') vector by an angle of θ_c . The rotation matrix is actually a matrix defining the coupling between the four quarks. It may be clearer to represent this matrix as follows

$$\begin{matrix} & d & s \\ u & \begin{pmatrix} \cos\theta_c & \sin\theta_c \\ -\sin\theta_c & \cos\theta_c \end{pmatrix} & \\ c & & \end{matrix} \quad (11)$$

Here we see that the u and d and the s and c pairs are coupled with a strength proportional to $\cos\theta_c$ and the u and s and the c and d pairs are coupled with a strength of $\sin\theta_c$ and $-\sin\theta_c$ respectively.

2.5 KM Theory and the CKM Matrix

In 1973, when the c quark had not even been firmly established, Kobayashi and Maskawa proposed a new model of quark mixing [13] which built upon Cabibbo's model. The Kobayashi-Maskawa (KM) theory took Cabibbo's theory and added two new quarks: the top (t) and bottom (b) quarks. Adding the two new quarks changed Cabibbo's 2-dimensional rotation matrix to a 3-dimensional complex rotation matrix. The new quark mixing equation was

$$\begin{pmatrix} d' \\ s' \\ b' \end{pmatrix} = \begin{pmatrix} V_{ud} & V_{us} & V_{ub} \\ V_{cd} & V_{cs} & V_{cb} \\ V_{td} & V_{ts} & V_{tb} \end{pmatrix} \begin{pmatrix} d \\ s \\ b \end{pmatrix}. \quad (12)$$

Where the rotation matrix is called the Cabibbo-Kobayashi-Maskawa (CKM) matrix and is defined as V , where

$$V \equiv \begin{pmatrix} c_{12}c_{13} & s_{12}c_{13} & s_{13}e^{-i\delta_{13}} \\ -s_{12}c_{23} - c_{12}s_{23}s_{13}e^{i\delta_{13}} & c_{12}c_{23} - s_{12}s_{23}s_{13}e^{i\delta_{13}} & s_{23}c_{13} \\ s_{12}s_{23} - c_{12}c_{23}s_{13}e^{i\delta_{13}} & -c_{12}s_{23} - s_{12}c_{23}s_{13}e^{i\delta_{13}} & c_{23}c_{13} \end{pmatrix}. \quad (13)$$

There are four parameters which define the CKM matrix: θ_{12} , θ_{13} , θ_{23} and δ_{13} . In (13), c_{ij} and s_{ij} are the cos and sin of θ_{ij} respectively. In the limit $\theta_{13} = \theta_{23} = 0$ the CKM matrix reduces to the Cabibbo mixing matrix with $\theta_c = \theta_{12}$. The matrix is also assumed to be unitary — which means $V^\dagger V = I$, where I is the identity matrix and V^\dagger is the Hermitian conjugate or the transpose of the complex conjugate of V . The current values of the CKM elements are [14] [* assumes unitarity]

$$V = \begin{pmatrix} .9739 \pm .0009 & .2200 \pm .0025 & .0035 \pm .0006 \\ .224 \pm .014 & .97 \pm .06 & .041 \pm .003 \\ .0083 \pm .0016 & .04 \pm .01^* & .99 \pm .15^* \end{pmatrix}. \quad (14)$$

Later, Wolfenstein approximated the CKM matrix [15], emphasizing the hierarchy in the size of the angles, $s_{12} \gg s_{23} \gg s_{13}$. Here we let $\lambda \equiv s_{12}$ and expand all the elements of the CKM matrix in terms of λ . The approximated CKM matrix is then

$$V \approx \begin{pmatrix} 1 - \lambda^2/2 & \lambda & A\lambda^3(\rho - i\eta) \\ -\lambda & 1 - \lambda^2/2 & A\lambda^2 \\ A\lambda^3(1 - \rho - i\eta) & -A\lambda^2 & 1 \end{pmatrix} \quad (15)$$

to order λ^3 . Where we use the four parameters A , ρ , λ and η instead of the θ_{ij} and δ_{13} . Of the four parameters, A and λ are well known; $A = .834 \pm .043$ and $\lambda = \sin\theta_c$.

The CKM matrix can also be represented as one of six “unitary triangles”. These triangles are geometrical representations of the unitarity condition imposed on the CKM matrix. If we impose the unitarity condition we get these six equations

$$\sum_{\alpha=d,s,b} V_{i\alpha} V_{j\alpha}^* = 0, \quad i \neq j \quad (16)$$

$$\sum_{i=u,c,t} V_{i\alpha} V_{i\beta}^* = 0, \quad \alpha \neq \beta. \quad (17)$$

If we draw these equations in the complex plane we get the triangles in Figure 3. The most common triangle used is a simplified version of the db triangle (Figure 4). In this simplified version, we choose to orient the triangle such that $V_{cd}V_{cb}^*$ lies along the x-axis because it is approximately real, we use the Wolfenstein approximation, we make the further approximation $1 - \lambda^2/2 \approx 1$

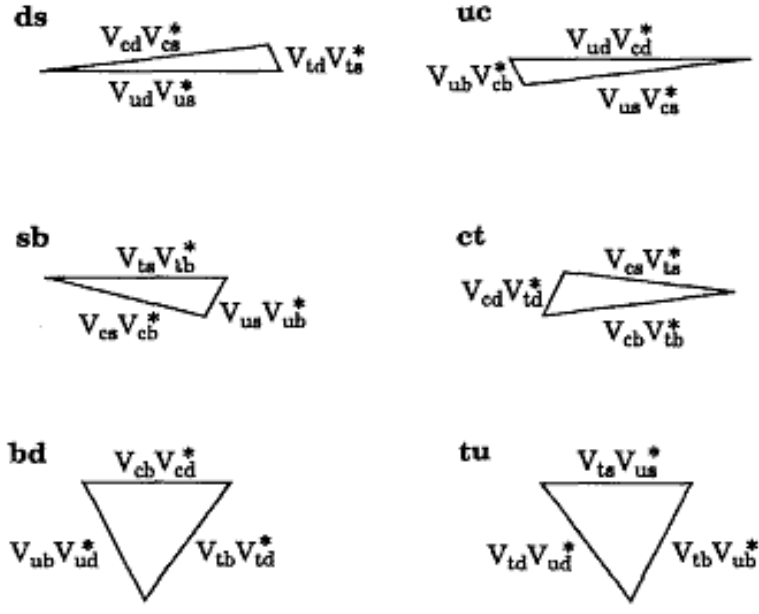


Figure 3: The six unitarity triangles as presented in [1]. The triangles on the left are from (17) and the ones on the right are from (16).

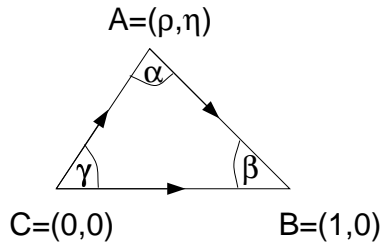


Figure 4: The simplified db unitarity triangle.

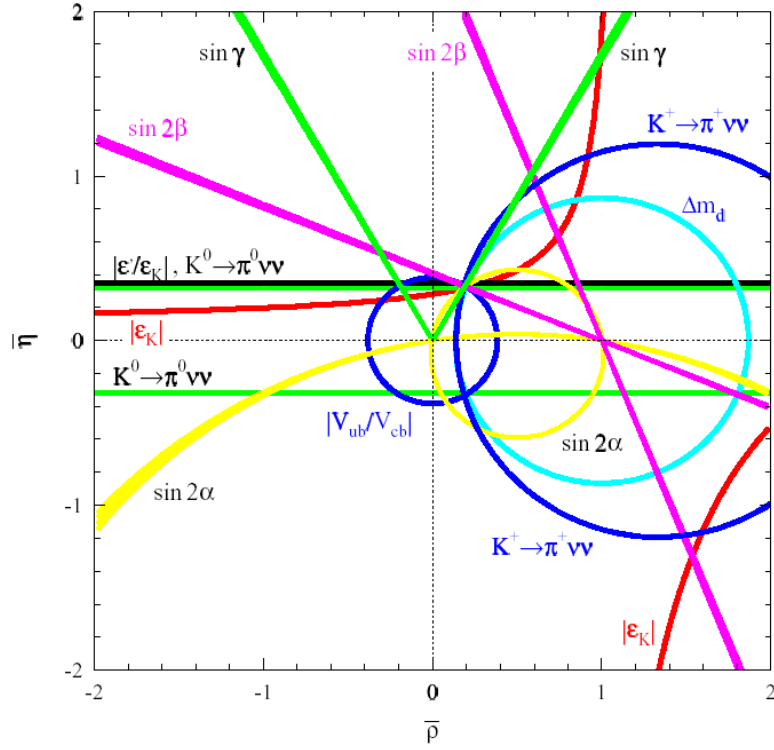


Figure 5: Constraints in the $(\bar{\rho}, \bar{\eta})$ plane for the most relevant observables as presented in [2].

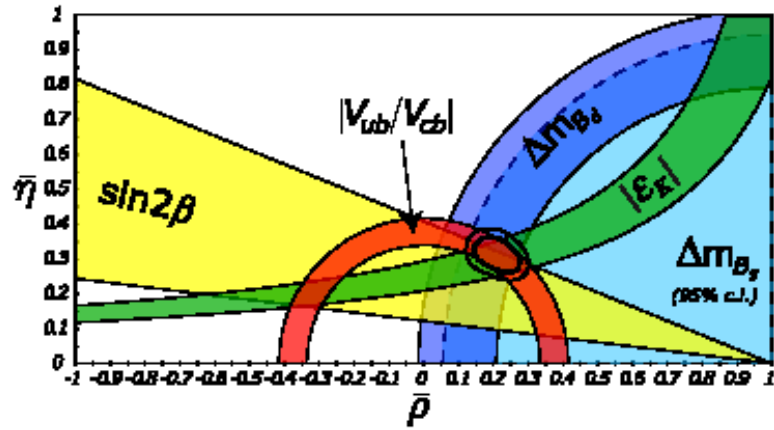


Figure 6: The current measured constraints on $\bar{\rho}$ and $\bar{\eta}$ as presented in [3].

and we rescale the triangle by a factor of $1/A\lambda^3$ to make the base unit length.

CP violation is extracted from the CKM matrix through the parameters. With several calculations, which we will not go into, it is found that

$$\epsilon = C_\epsilon B_K \lambda^6 \bar{\eta} [C_1 A^2 \lambda^4 (1 - \bar{\rho}) + C_2 + C_3] \quad (18)$$

$$\left| \frac{\epsilon'}{\epsilon} \right| \propto \eta \quad (19)$$

where

$$\bar{\eta} = \eta \left(1 - \frac{\lambda^2}{2}\right) \quad (20)$$

$$\bar{\rho} = \rho \left(1 - \frac{\lambda^2}{2}\right). \quad (21)$$

We will not discuss the rest of the variables in (18) as they are not important for this discussion. The parameters ρ and η are not well measured. There are several ways to measure them (as illustrated in Figure 5), including using (18) and (19). The current measurements are drawn in Figure 6.

3 The CKM Experiment

Charged Kaons at the Main-Injector (CKM) [16] is a fixed target, high-energy physics experiment that is proposing to measure $|V_{td}|$ to 10% by directly measuring $\Gamma(K^+ \rightarrow \pi^+ \nu \bar{\nu})$. An international collaboration of more than 40 physicists hope to run the CKM experiment at Fermi National Accelerator Laboratory (FNAL) in 2006 for two years. CKM was granted Scientific (Stage I) approval on June 28, 2001; there is one more stage before CKM will get to run. They expect to put a constraint on (ρ, η) as depicted in Figure 7.

The CKM experiment plans to use a 50MHz, separated, $\sim 22\text{GeV}/c$ K^+ beam. The kaons will decay in flight in a $\sim 30\text{meter}$ decay region. The detector has redundant measurements of velocity and momentum for both the incoming K^+ and the outgoing decay products using conventional magnetic spectrometers and phototube ring imaging Cherenkov counters. The detector also consists of a hermetic photon veto system and a muon range stack. The detector is pictured in Figure 8.

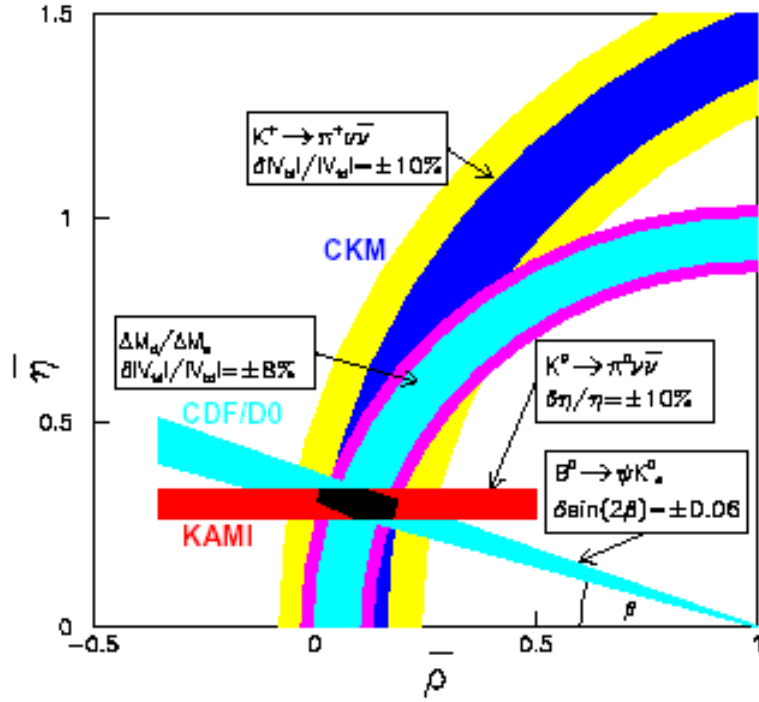


Figure 7: A possible outcome for constraints on $\bar{\rho}$, $\bar{\eta}$ and β obtained from future experiments, as presented in [3].

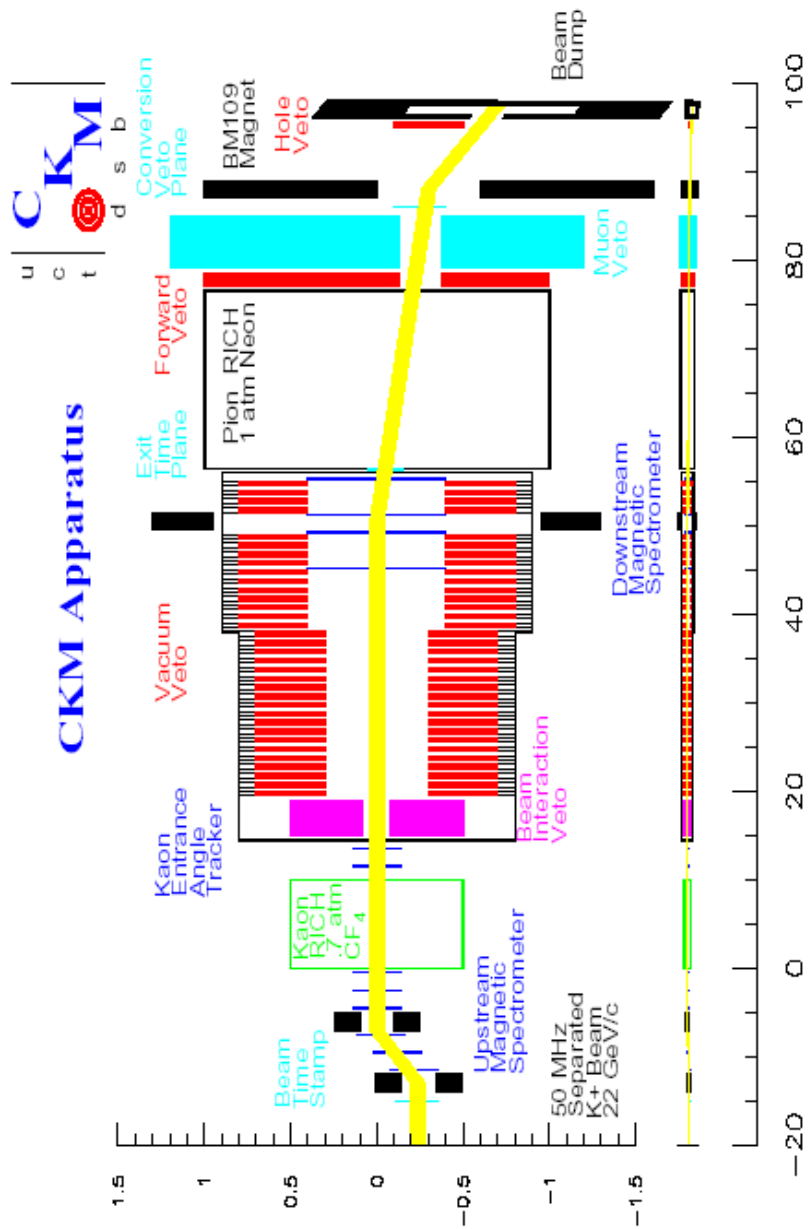


Figure 8: The CKM detector as presented in [3]. The lower section (when viewed as landscape) shows the true proportions of the detector.

3.1 The DMS

The downstream magnetic spectrometer (DMS) is composed of straw tubes. A CKM straw tube consists of a thin walled (~ 1 mil thick), .5cm diameter, 80cm long, kapton tube with 100nm of copper deposit on the inside of the tube. A $20\mu\text{m}$ diameter, gold plated, tungsten wire is strung inside the straw tube and centered. There is a $\sim 1800\text{V}$ potential difference between the straw tube and the wire. The straw is also filled with a gas, such as CF_4 -isobutane or CF_4 -ethane. When a charged particle goes through the tube, it will strip electrons off some the gas molecules and leave a trail of ionization in the tube. The free electrons will drift towards the wire and send a pulse to some electronics which will record that pulse as a hit. The ions will drift towards the straw tube and return to their neutral state by picking up an electron from the tube. Through analysis of the hits, a CKM straw tube can measure particle positions with $150\mu\text{m}$ resolution.

The DMS is used for tracking and measuring momentum of particles. It consists of 29 layers of straw arrays grouped into four sections called straw drift chambers, or DMS chambers. A straw array is a row of 160 parallel straws lined up in a single plane of view with no gaps between tubes. Two drift chambers are on each side of a .333Tesla (100MeV/c pt kick) dipole magnet with $\sim 2.5\text{m}$ spacing between chambers, as shown in Figure 8. The first drift chamber (DMS1) has five layers of straws labeled X,X',Y,Y' and U. The second, third and fourth chambers (DMS2-4) have 8 layers of straws each, labeled X,X',Y,Y',U,U',V and V'. A layer and its primed counterpart are offset by a straw radius and placed on top of each other (Figure 9). The Y, U and V views are rotated from the X view by 90° , -45° and 45° respectively.

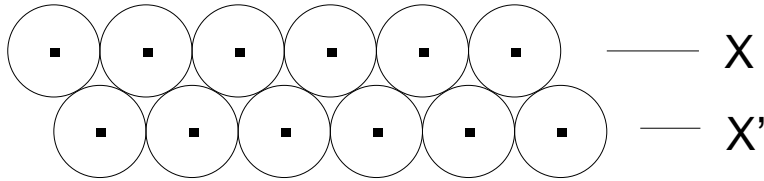


Figure 9: Two layers of straws, one primed and one unprimed, seen from end on. The dot in the center of each tube is the wire.

4 Pattern Recognition in the DMS

In order to do tracking and momentum calculations with the DMS data, software must be written to recognize patterns in the data and generate particle tracks through the detector. Other parts of the detector can then use these tracks to analyze the event further. We wrote pattern recognition code to run off of data from a Monte Carlo (Geant) simulation. The simulated data uses single K^+ events where the K^+ does not decay. The particles all start off with $p_z = p = 22\text{GeV}/c$ and have an (x,y) starting position randomly distributed throughout a 40cm radius circular area 6m before the first DMS chamber.

4.1 The Algorithm

The Algorithm we used to take the raw DMS data and generate particle tracks consists of grouping hits into larger and larger groups until a group constitutes a track. We first take the raw DMS simulated output, which includes the track number, particle type, x, y and z positions, x momentum / total momentum (p_x/p), y momentum / total momentum (p_y/p), z momentum / total momentum (p_z/p), total momentum (p), time of flight, straw layer number, wire number and momentum loss for each DMS hit, and turns it into data that is similar to what an actual detector might output, called digitized data. The digitized data includes the straw layer number, wire number and drift distance for each hit.

Drift distance is defined as the minimum distance between the wire and the track for a particular straw. To find the drift distance we need to know the positions of all the wires. The software is supplied with a wire position table that gives the straw layer number, wire number, z position and position along the view axis for each wire. The table is hard coded into a separate file and will never change over the course of the experiment. Using the wire position table and the x and y positions of a hit, we can find the drift distance by taking the absolute value of the view position calculated from x and y minus the view position given by the wire position table for that wire. To find the position for the U and V views given the x and y position, we used the equations

$$u = \frac{x + y}{\sqrt{2}} \tag{22}$$

$$v = \frac{x - y}{\sqrt{2}} \quad (23)$$

For example, for the U view, we have

$$drift\ distance = \left| \frac{x + y}{\sqrt{2}} - (u\ position\ from\ table) \right| \quad (24)$$

We also have to smear the drift distances because the simulated data has no error but, the actual DMS data will have $150\mu\text{m}$ resolution. Smearing a number means adding on a small amount to the number to account for an error. To smear the drift distance we need to add a number that is distributed with a gaussian distribution around 0, and has $\sigma=150\mu\text{m}$. We used a function called “white_noise,” which takes a variance (σ^2) and returns the desired random number. We tested this function’s accuracy by plotting a histogram of 100,000 randomly distributed numbers with $\sigma=150\mu\text{m}$ (Figure 10). The gaussian fit to the histogram shows that the standard deviation of the fit is consistent with $150\mu\text{m}$ within $.3\sigma$ and the mean is consistent with 0 to 1.88σ . Since the mean is 10^{-3} time smaller than standard deviation and the standard deviation of the fit is so close to $150\mu\text{m}$, the “white_noise” function will give us a well distributed random number.

Now that we have the digitized data, we start grouping the hits from the pairs of primed and unprimed layers. For each pair, we loop through all the hits in the unprimed layer and try to match it with a hit from the primed layer to create a valid hit pair (VHP). To be a VHP, the two hits must be in two adjacent straws and the sum of the drift distances must equal the straw radius within a constant (call it C). The sum of the drift distances will not equal the straw radius exactly because of the position resolution, the angle of the track and multiple scattering. Multiple scattering is when a particle hits some material and is deflected. To find C, we plot a histogram of $|(\sum\ drift\ distance) - (straw\ radius)|$ for $\sim 56,000$ pairs (Figure 11). For the purposes of this study, we want the highest track finding efficiencies as possible, so we set $C=5\sigma$ so that all of the pairs will be accepted. In this case $C=.104\text{cm}$.

After we find each VHP, we mark the hits but, we keep all VHPs whether some hits belong to more than one VHP or not. After finding all VHPs, we go through all the hits and classify all of the single hits that were not marked as VHPs. We call them VHPs yet we do not know which side of the wire the track was on; the drift distance is an unsigned quantity. We solve this

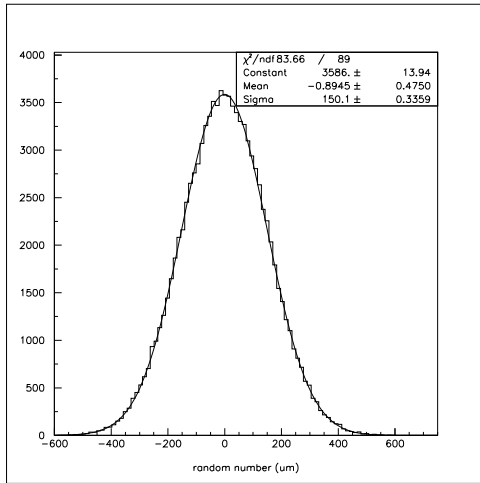


Figure 10: 100,000 randomly distributed numbers using “white_noise”.

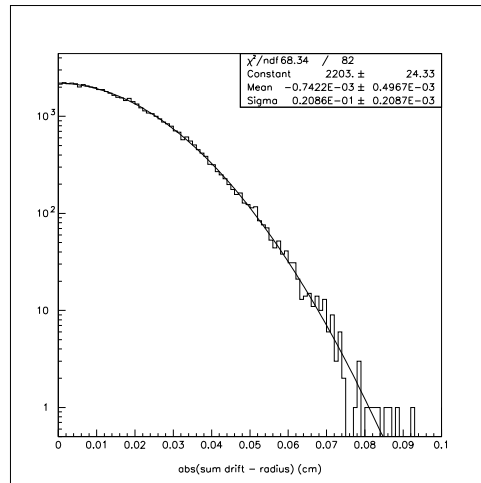


Figure 11: A histogram of $|\left(\sum drift\ distance\right) - (straw\ radius)|$ for $\sim 56,000$ pairs of hits, fit to a gaussian distribution.

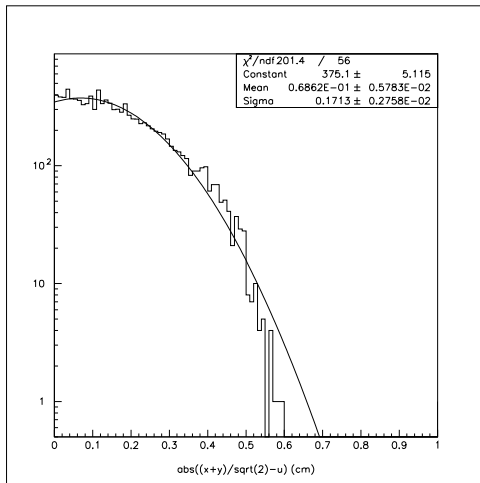


Figure 12: A histogram of $\left|\frac{x+y}{\sqrt{2}} - u\right|$ for $\sim 10,000$ good DMS crossing, fit to a gaussian distribution.

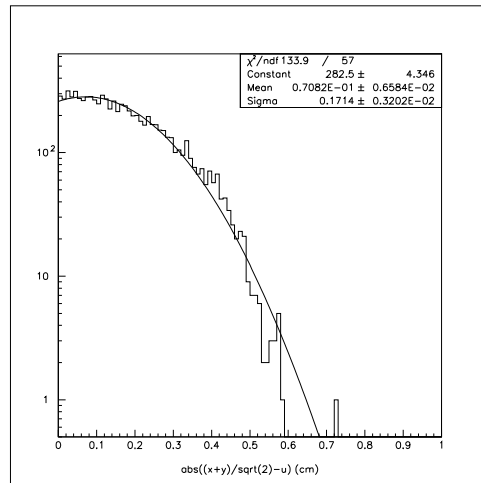


Figure 13: A histogram of $\left|\frac{x-y}{\sqrt{2}} - v\right|$ for $\sim 8,000$ good DMS crossing, fit to a gaussian distribution.

problem later in the algorithm. For the VHPs with two different hits, we do know which side of the wire the track was on because the straw tubes in the primed layers are staggered by a straw radius from the tubes in the unprimed layers and we will never see a track which goes on the same side of both wires; $|pz| \gg |px|$ and $|pz| \gg |py|$.

Next, we group VHPs into groups called DMS crossings taking one VHP per view. For each DMS chamber, we loop through all combinations of VHPs, one from each view, and make cuts to find the best DMS crossings. For all the DMS chambers, we first make a quick cut on how close the x and y hits match up to the u hits. We cut on $|\frac{x+y}{\sqrt{2}} - u| < C_1$. Using $\sim 10,000$ good DMS crossings, we plot a histogram (Figure 12) and, to obtain the highest track finding efficiencies, we let $C_1 = 5\sigma = .857\text{cm}$. Then, for DMS2-4, we have another quick cut on how close the x and y hits match up to the v hits; we cut on $|\frac{x-y}{\sqrt{2}} - v| < C_2$. Using $\sim 8,000$ good DMS crossings we find (Figure 13) $C_2 = 5\sigma = .857\text{cm}$, which is the same as C_1 , as expected. Next, we look at any VHPs with a single hit that are used in the DMS crossing and use the VHPs from the other views to figure out which side of the wire the track went on.

Then, we calculate a least squares average over all the hits in the DMS crossing to find one space point (x,y,z) for the entire DMS crossing. First, we need to minimize the χ^2 equation

$$\chi^2 = \sum_{i=x \text{ hits}} \frac{(x - x_i)^2}{\sigma_i^2} + \sum_{i=y \text{ hits}} \frac{(y - y_i)^2}{\sigma_i^2} + \sum_{i=u \text{ hits}} \frac{(\frac{x+y}{\sqrt{2}} - u_i)^2}{\sigma_i^2} + \sum_{i=v \text{ hits}} \frac{(\frac{x-y}{\sqrt{2}} - v_i)^2}{\sigma_i^2} \quad (25)$$

to find the x and y positions of the space point and use

$$z = \frac{\sum_{i=all \text{ hits}} z_i}{number \ of \ hits} \quad (26)$$

to find the z position of the space point because the errors on z_i are all the same. Next, we place the values of the space point back into (25) to calculate the χ^2 and divide by the degrees of freedom (number of hits - number of parameters) to obtain the χ^2 per degree of freedom ($\chi^2/degree$) of the fit. We can make the cut $\chi^2/degree < C_3$ for DMS1 and $\chi^2/degree < C_4$ for DMS2-4 by first making a histogram of the $\chi^2/degree$ for DMS1 (Figure 14) and for DMS2-4 (Figure 15) using ~ 3000 events with 29 hits. We separate the two plots instead of superimposing them because DMS1 has fewer straw

layers than DMS2-4 so we expect the $\chi^2/degree$ distributions to be different. Looking at the plots, we decide to make very loose cuts of $C_3=8$ and $C_4=10$ in order to accept all of the good events.

The last step in choosing DMS crossings takes place after all combinations of DMS crossings have been found. We take all of the DMS crossings and order them by their value of $\chi^2/degree$. Then, we automatically accept the DMS crossing with the smallest $\chi^2/degree$ and mark the hits used in that DMS crossing. Next, we take the DMS crossing with the next smallest $\chi^2/degree$ and if any of the hits used in this DMS crossing are already marked, we reject it. If none of the hits used in the DMS crossing are marked, then we accept the crossing and mark all the hits used in the crossing. We repeat this process for all of the DMS crossings.

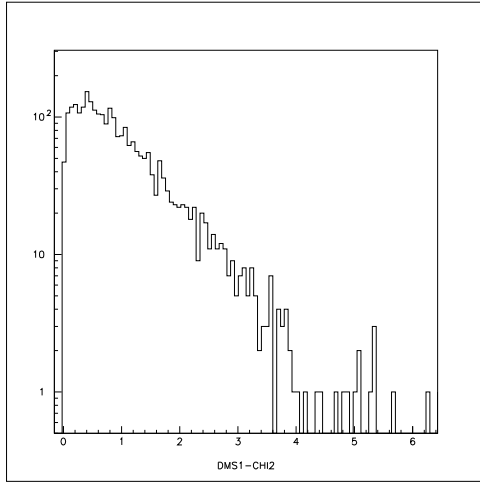


Figure 14: $\chi^2/degree$ distribution for DMS1.

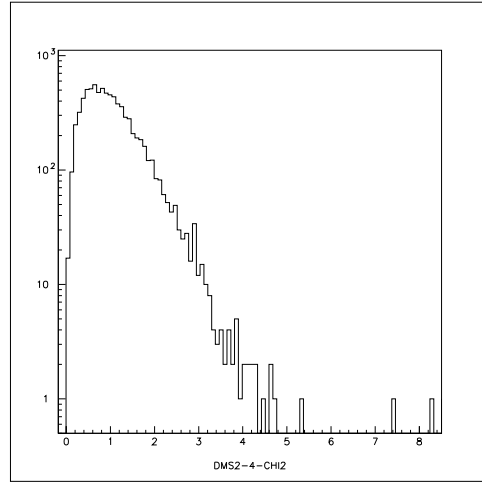


Figure 15: $\chi^2/degree$ distribution for DMS2-4.

To obtain the highest track finding efficiencies, we want to find tracks that may not have left hits in the unprimed and primed layers of a single view. To do this, we have another stage to find DMS crossings where we search for DMS crossings with exactly one view missing using only the hits that were not marked in the last step of the algorithm. For DMS1, we just loop through all combinations of hits from all combinations of two different views and accept every combination. For DMS2-4, we use a modified version of the three view DMS1 crossing finding algorithm where we run the algorithm for all combinations of three views.

Finally, we group one DMS crossing from each DMS chamber to form groups of hits called tracks. We loop through all combinations of DMS crossings and make three cuts. First, the slopes of the track between DMS chambers in the x-z plane must be decreasing or increasing. In other words, let M_{ij} be the slope of the track in the x-z plane between DMS i and DMS j , the cut is that $M_{12} < M_{23} < M_{34}$ or $M_{12} > M_{23} > M_{34}$.

Next, we fit the track to the equations

$$\chi_x^2 = \frac{(B_x - x_1)^2}{\sigma_{x_1}^2} + \frac{(B_x + M_x(z_2 - z_1) - x_2)^2}{\sigma_{x_2}^2} + \frac{(B_x + M_x(z_3 - z_1) + C(z_3 - z_m) - x_3)^2}{\sigma_{x_3}^2} + \frac{(B_x + M_x(z_4 - z_1) + C(z_4 - z_m) - x_4)^2}{\sigma_{x_4}^2} \quad (27)$$

$$\chi_y^2 = \frac{(B_y - y_1)^2}{\sigma_{y_1}^2} + \frac{(B_y + M_y(z_2 - z_1) - y_2)^2}{\sigma_{y_2}^2} + \frac{(B_y + M_y(z_3 - z_1) - y_3)^2}{\sigma_{y_3}^2} + \frac{(B_y + M_y(z_4 - z_1) - y_4)^2}{\sigma_{y_4}^2} \quad (28)$$

where B_i is the i intercept at $z=(z \text{ of } DMS_i)$, M_i is the slope of the track in the i -z plane before the magnet, C is the change in slope from before and after the magnet, z_m is the z position of the center of the magnet and σ_{i_j} is the error on the i position of the space point used from DMS j . We can separate the χ_x^2 and the χ_y^2 because the motion of the particle in the y-z plane is independent from the motion of the particle in the x-z plane to an exceptional approximation. (27) and (28) fits the track to a line before z_m and a line after z_m where the two lines are joined at z_m . The track really is a straight line before and after the magnetic field and a helix inside the magnetic field, but the radius of curvature of the helix is so large that (27) and (28) are excellent approximations.

To find good tracks we want to cut on the χ^2/degree of the track and the calculated momentum (p). First we cut on $p < C_5$. We use the equation

$$p = \frac{(-.2998 \text{ GeV}/cT)Bl_m}{C\sqrt{1 + \frac{M_y^2}{1+M_x^2}}} \quad (29)$$

to calculate p. In (29), B is the magnetic field of the magnet and l_m is the length of the magnet. To find C_5 we want the upper limit of reconstructed particle momentums. We plot a histogram of initial particle momentums from a simulated CKM beam (Figure 16) and then generate ~ 4000 events with initial momentums equal to the highest momentum in Figure 16 (23GeV/c). We then take those events and produce a histogram of reconstructed momentums (Figure 17). We see that $C_5 = \mu + 5\sigma = 24.47$.

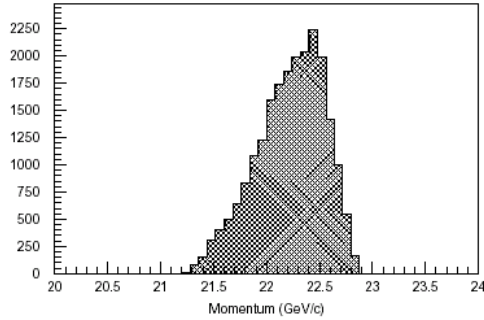


Figure 16: Initial particle momenta from a simulated CKM beam as obtained from [3].

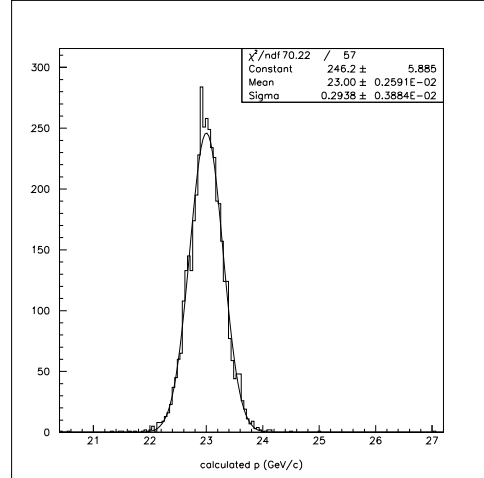


Figure 17: Histogram of reconstructed momenta of ~ 4000 events with initial momentum of $23\text{GeV}/c$.

To cut on the χ^2/degree of the track we first cut on $\chi_y^2/\text{degree} < C_6$ because we need to calculate χ_y^2/degree eventually and it is easier to calculate than χ_x^2/degree . We then cut on $\chi^2/\text{degree} < C_7$ using $\chi^2 = \chi_y^2 + \chi_x^2$. To find C_6 and C_7 , we plot histograms of χ_y^2/degree and χ^2/degree for ~ 3000 good events with 29 hits per event in Figures 18 - 21. Here, we see that some of the events have very large χ^2/degree values. If we look at the raw simulated data for the events with $\chi^2 > 100$, we see that every event has a large momentum shift (larger than $75\text{ MeV}/c$) due to multiple scattering off of material on the outside walls of the decay region. We would like to accept these events even though they have such large χ^2 values so we make a very loose cut and let $C_6 = C_7 = 10,000$.

Now that we have all the possible tracks, we want to weed out the fake tracks (tracks that did not occur in the raw simulated data) and keep all the good tracks that we can. We apply the same algorithm when choosing DMS crossings. We sort all the tracks by their χ^2/degree and automatically accept the track with the smallest χ^2/degree . Then, we mark the DMS crossings used in the track. Next, we accept the track with the next smallest χ^2/degree if none of the DMS crossings used in the track have been marked. If the track is accepted, we mark the DMS crossings used and go on to the next track.

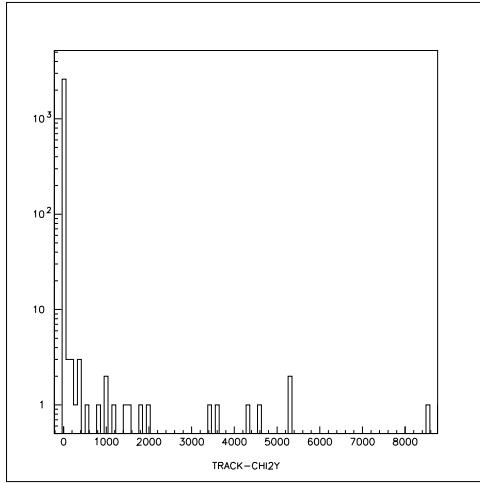


Figure 18: $\chi^2_y/degree$ distribution for ~ 3000 good events with 29 hits per event.

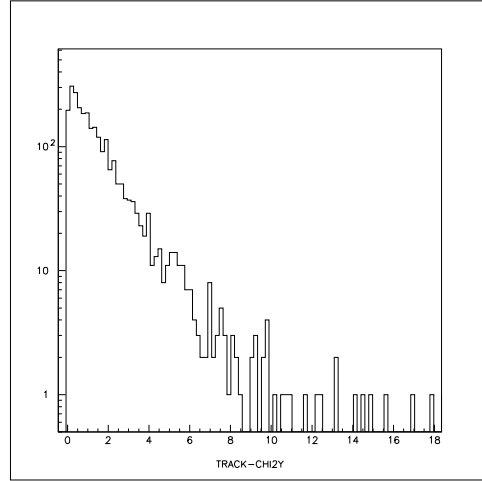


Figure 19: Close up of Figure 18.

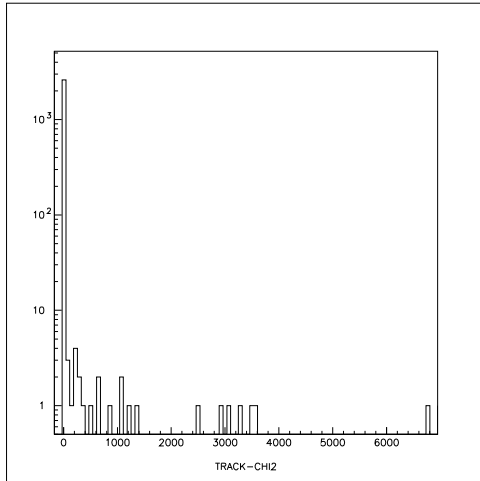


Figure 20: $\chi^2/degree$ distribution for ~ 3000 good events with 29 hits per event.

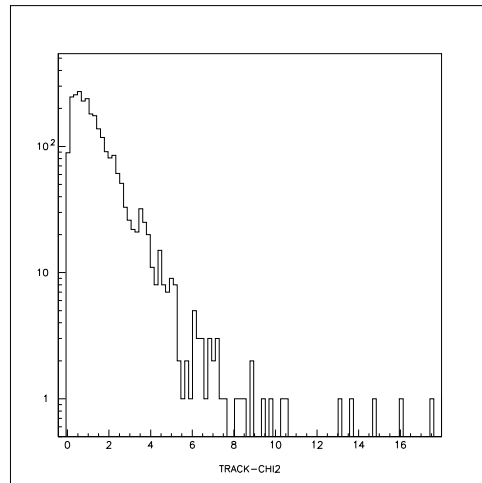


Figure 21: Close up of Figure 20.

This last step completes the algorithm and gives us a reliable list of tracks.

4.2 Results

4.2.1 Momentum Resolution

Now that we have an algorithm designed to find particle tracks, we can take these tracks and see how well we can measure the average momentum of the particle over the length of the track. We calculated the momentum of each track using 29 and compared it to the average momentum of the actual Geant generated track for ~ 5000 tracks (Figure 22). Here, we get $\sigma = .2621 \pm .003410$ which gives us a momentum resolution of $1.191 \pm .0155\%$. This is very close to the momentum resolution of $\sim 1\%$ proposed by the CKM collaboration [3].

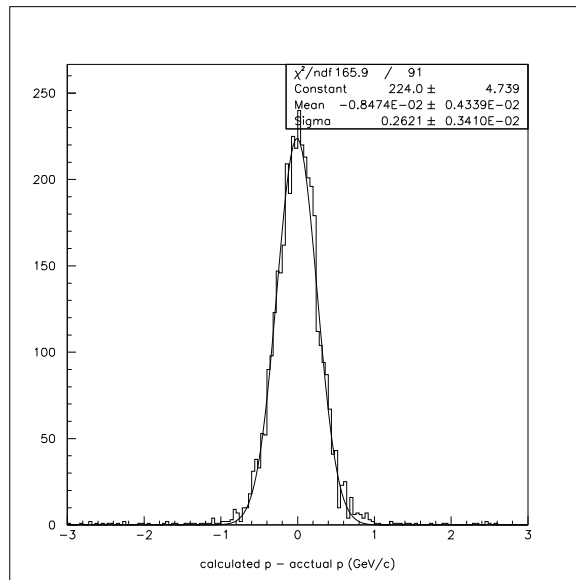


Figure 22: Histogram of (calculated p - average actual p) for ~ 5000 tracks.

4.2.2 Track Finding Efficiency

The most important requirement of the algorithm is that it must have good track finding efficiency. The ability to find a track depends upon two major things: how many hits are in the track and where the track is in the detector.

If the track only has 5 hits in DMS1 and 8 hits in DMS2 and no other hits, then the algorithm will not find the track. Also, if there are 116 hits in an event (enough for 4 tracks), there is a good chance a combination of hits can pass cuts and yet not be an actual track. If the track is near the outside of the beam pipe, it is more likely to hit the outer edge of the beam pipe, where there is a significant amount of material, and scatter. The track can also enter a dead region in the middle of the beam pipe, where the straws are turned off, and hit dead straws giving no hits in the data.

We took events with one, two and four kaons per event and plotted the track finding efficiency versus number of hits per event (Figures 23 - 25). To calculate the efficiency for a particular “number of hits per event” bin, we summed up all the tracks found, in which every hit belonged to the same generated track found in the raw data, and divided by the total number of tracks generated. These are very good efficiencies. Most of the low efficiencies are a result of the event not having enough hits to satisfy certain cuts.

The reason for the low efficiencies is that there is a high inefficiency in events with a small number of hits per event due to the particle hitting the outer wall of the beam pipe. We plotted the track finding inefficiency due to particles hitting the outer wall versus the number of hits per event (Figure 26). A track is considered to hit the wall of the detector if the hit in its highest straw plane is outside of a 38cm radius circle centered at (0,0). Tracks with a small number of hits have such few hits because they hit the outer wall and stop or scatter.

There is also an inefficiency associated with particles entering the dead region in the middle of the pipe. The dead region is a 5cm radius circle centered at the center of the particle beam at each straw plane. This is so that particles that go through the detector without decaying do not register any hits. Since the dead region follows the beam path, we do not expect to see many particles enter or leave the dead region unless they are significantly scattered. We measured the track finding inefficiency due to the dead region for ~ 5000 particles and we did not find a single particle which entered or left the dead region.

4.2.3 Timing

One important property of any program used in a high energy physics experiment is that the program must be fast. If the program took one second to analyze one event and the experiment had one computer running the pro-

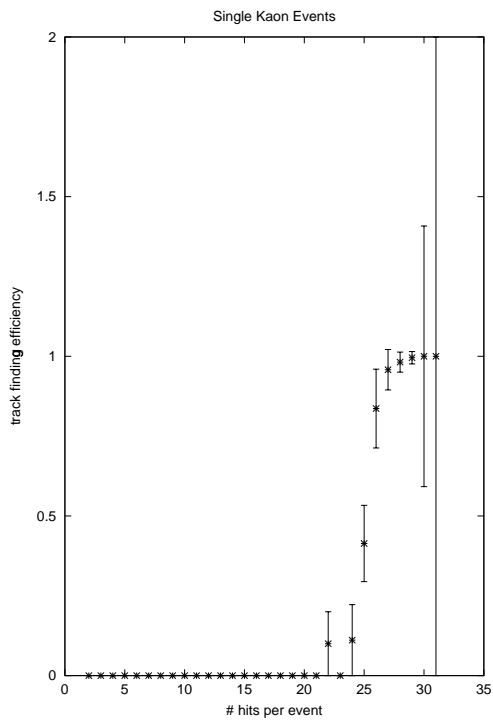


Figure 23: Track finding efficiency of 4400 events with one kaon per event.

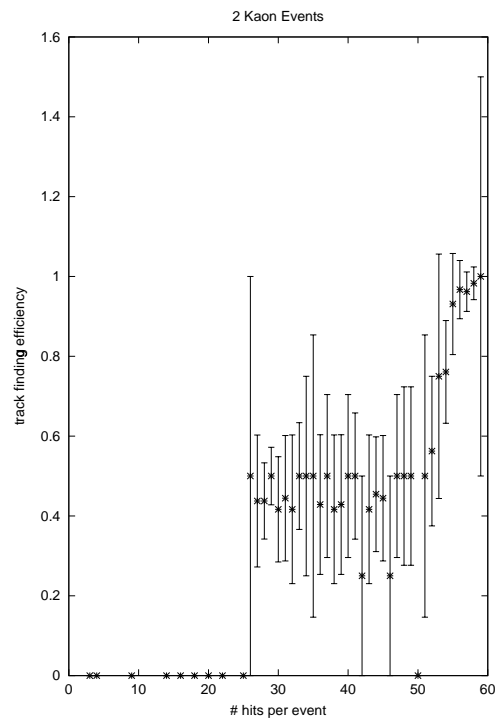


Figure 24: Track finding efficiency of 1000 events with two kaons per event.

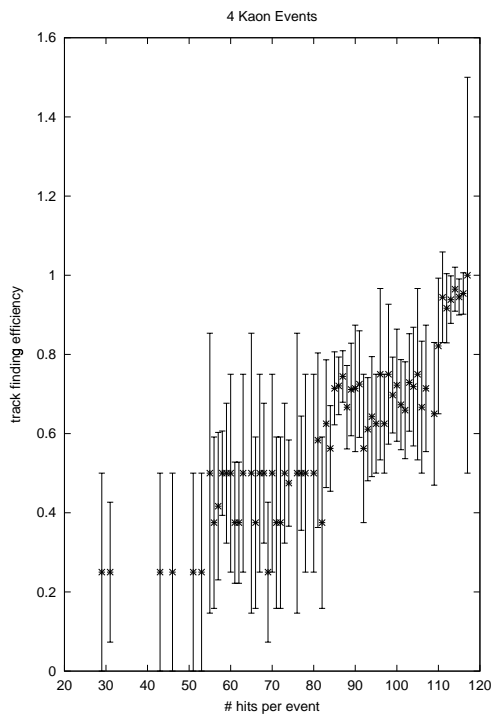


Figure 25: Track finding efficiency of 1000 events with four kaons per event.

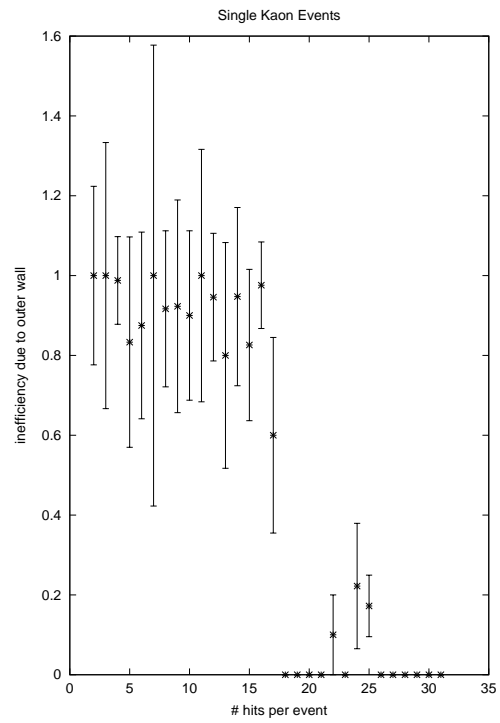


Figure 26: Track finding inefficiency due to particles hitting the outer wall of the beam pipe.

gram, then it would take years just to analyze all the data taken from just a few hours worth of data collection. For the program to be fast, the algorithm must be fast. We measured the speed of the algorithm for each 'number of hits per event' bin and plotted the results in Figure 27.

The timing for any program depends on which computer is used, so these times are rough estimates of the kinds of times we should expect during the actual CKM experiment. The plot does, however, show how the time of the algorithm increases with the number of hits per event. After fitting the data to several different equations, the one with the best fit is the exponential. This means that the algorithm most likely has exponential runtime, or is $O(e^n)$, where n is the number of hits per event.

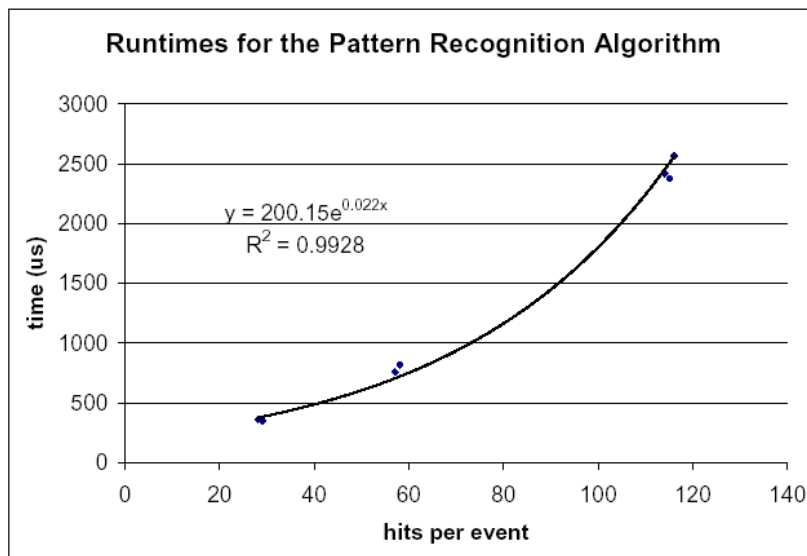


Figure 27: Average runtime vs. the number of hits per event. The data is fit to an exponential; the equation of the fit is on the graph.

References

- [1] R. Aledsan, B. Kayser, and D. London. Determining the Quark Mixing Matrix from CP-violating Asymmetries. *Phys. Rev. Lett.*, 73(1):18–20, July 1994.
- [2] A. Höcker and H. Lacker and S. Laplace and F. Le Diberder. A New Approach to a Global Fit of the CKM Matrix. Accepted for publication in *The European Physical Journal C*, may 2001.
- [3] CKM Collaboration. Charged Kaons at the Main Injector. A Proposal for a Precision Measurement fo the Decay $K^+ \rightarrow \pi^+ \nu \bar{\nu}$ and Other Rare K^+ Processes at Fermilab Using the Main Injector, April 2001.
- [4] G. D. Rochester and C. C. Butler. *Nature*, 160:855–857, 1947.
- [5] T. Nakano and K. Nishijima. *Prog. Theor. Phys.*, 10:581–582, 1953.
- [6] M. Gell-Mann. *Phys. Rev.*, 92:833–834, 1953.
- [7] M. Gell-Mann and A. Pais. *Phys. Rev.*, 97:1387–1389, 1955.
- [8] K. Lande, E. T. Booth, J. Impeduglia, and L. M. Lederman. *Phys. Rev.*, 103:1901–1904, 1956.
- [9] J. H. Christenson, J. W. Cronin, V. L. Fitch, and R. Turlay. Evidence for the 2π Decay of the K_2^0 Meson. *Phys. Rev. Lett.*, 13(4):138–140, July 1964.
- [10] *The European Physical Journal C*, 15(1–4), 2000.
- [11] N. Cabibbo. Unitary Symmetry and Leptonic Decays. *Phys. Rev. Lett.*, 10(12):531–533, June 1963.
- [12] S. L. Glashow, J. Iliopoulos, and L. Maian. Weak Interactions with Lepton-Hadron Symmetry. *Phy. Rev.*, 2(7):1285–1292, October 1970.
- [13] M. Kobayashi and T. Maskawa. *Prog. Theor. Phys.*, 49:652, 1973.
- [14] B. Heltsley. CKM Status and Prospects. Talk at Physics in Collision, Cornell University, June 29, 2001.

- [15] L. Wolfenstein. Parametrization of the Kobayashi-Maskawa Matrix. *Phys. Rev. Lett.*, 51(21):1945–1947, November 1983.
- [16] The CKM Collaboration. CKM (E921) WWW Server. World Wide Web, <http://www.fnal.gov/projects/ckm/Welcome.html>, 2001.